Compressible turbulent channel and pipe flow: similarities and differences

SOMNATH GHOSH[1], HOLGER FOYSI[2] AND RAINER FRIEDRICH[1]†

[1]Lehrstuhl für Aerodynamik, TU München, Boltzmannstrasse 15, D-85748, Garching, Germany

[2]Aerodynamisches Institut, RWTH Aachen, Wuellnerstrasse 5a, D-52062, Aachen, Germany

Direct numerical simulation (DNS) is used to explore similarities and differences between fully developed supersonic turbulent plane channel and axisymmetric non-swirling pipe flow bounded by isothermal walls. The comparison is based on equal friction Mach number, friction Reynolds number, Prandtl number, ratio of specific heats and viscosity exponent. The channel half-width and pipe radius are chosen to define the Reynolds numbers. To what extent and why mean flow quantities, second-order turbulence statistics and terms in the Reynolds stress equations coincide or diverge in both flows are investigated. The role of the fluctuating pressure in causing characteristic differences among correlations involving pressure fluctuations is identified via a Green-function-based analysis of the pressure field.

1. Introduction

Compressible wall-bounded turbulent flows are an important element of high-speed flight. They appear both in external flows over aerospace vehicles and in engine inlets and combustors. Although compressible wall-bounded turbulence has attracted researchers since the fifties of the last century, the underlying phenomena are not understood in all respects, even today. Early experimental evidence on compressible wall-bounded shear flows has been discussed by Bradshaw (1977), Fernholz & Finley (1976) and Kline, Cantwell & Lilley (1982). Lele (1994), Chassaing *et al.* (2002), Smits & Dussauge (2006) and Gatski & Bonnet (2009) have provided competent reviews on later experimental and numerical work.

It was the direct numerical simulations (DNS) of supersonic turbulent channel flow by Coleman, Kim & Moser (1995) and the companion work of Huang, Coleman & Bradshaw (1995) on data analysis and modelling issues which contributed to a better understanding of 'compressibility' effects in the form of mean property variations in shear flows bounded by isothermal walls. Nearly a decade later Foysi, Sarkar & Friedrich (2004) gave an explanation for the reduction of pressure–strain correlations in supersonic compared to incompressible isothermal channel flow by relating it to the sharp wall-normal density variations in the framework of a Green-function-based analysis of the pressure field. It was then natural to ask whether analogous effects

† Email address for correspondence: r.friedrich@lrz.tum.de

also hold in compressible flows through pipes and what the similarities or differences are between the channel and pipe flow.

Comparisons between incompressible turbulent channel and pipe flow have been performed earlier. However, they were focused on mean velocity profiles, friction laws and a few higher order statistics only. Schlichting (1968) drew attention to the similarity between velocity profiles of incompressible turbulent channel and pipe flow, but was aware of the fact that this similarity is not perfect. Nieuwstadt & Bradshaw (1997) used DNS data to show that the similarity fails beyond the second-order moments and offered an explanation based on a simple model. Wosnik, Castillo & George (2000) presented a theory of the mean velocity and skin friction for fully developed turbulent channel and pipe flow including Reynolds number effects. Nickels (2004) developed a functional form for the velocity profile of turbulent wall-bounded shear flow subjected to a strong pressure gradient which is based on the concept of a universal critical Reynolds number for the sublayer.

It is our objective to identify similarities and differences between fully developed compressible channel and pipe flow up to second-order turbulence statistics and to provide explanations for the corresponding behaviour based on an analysis of the Reynolds stress balances and the pressure field. The results may also motivate work on differences and similarities of other turbulent flows, e.g. plane and axisymmetric free shear flows.

The paper is organized as follows. The governing equations for DNS of compressible turbulent flow of a thermally perfect gas in cylindrical coordinates are presented in §2, together with the values for the flow parameters characterizing fully developed pipe and channel flow. The high-order numerical schemes, computational domain sizes and grid resolutions used are discussed as well. Section 3 is devoted to the comparison of mean momentum and energy balances in pipe and channel flow, to the resulting consequences for profiles of mean flow variables and to the exposure of similarities and differences in second-order moments. In §4, deeper insight into subtle differences between the pipe and channel flow is gained from an analysis of the four Reynolds stress budgets. An attempt is made in §5 to explain differences in the pressure–strain correlations, based on a Green's function analysis of the pressure fluctuations. Finally, conclusions are drawn in §6.

2. Details of direct simulations

The governing equations for compressible flow of a thermally and calorically perfect gas read in cylindrical (x, r, ϕ) coordinates (Bird, Stewart & Lightfoot 1960):

$$\frac{\partial \rho}{\partial t} + \frac{\partial \rho u_x}{\partial x} + \frac{1}{r}\frac{\partial r \rho u_r}{\partial r} + \frac{1}{r}\frac{\partial \rho u_\phi}{\partial \phi} = 0, \tag{2.1}$$

$$\frac{\partial \rho u_x}{\partial t} + \frac{\partial \rho u_x u_x}{\partial x} + \frac{1}{r}\frac{\partial r \rho u_x u_r}{\partial r} + \frac{1}{r}\frac{\partial \rho u_x u_\phi}{\partial \phi} = -\frac{\partial p}{\partial x} + \underbrace{\frac{\partial \tau_{xx}}{\partial x} + \frac{1}{r}\frac{\partial r \tau_{xr}}{\partial r} + \frac{1}{r}\frac{\partial \tau_{x\phi}}{\partial \phi}}_{V_x} + f_x, \tag{2.2}$$

$$\frac{\partial \rho u_r}{\partial t} + \frac{\partial \rho u_r u_x}{\partial x} + \frac{1}{r}\frac{\partial r \rho u_r u_r}{\partial r} + \frac{1}{r}\frac{\partial \rho u_r u_\phi}{\partial \phi} - \frac{\rho u_\phi^2}{r} = -\frac{\partial p}{\partial r}$$

$$+ \underbrace{\frac{\partial \tau_{xr}}{\partial x} + \frac{1}{r}\frac{\partial r \tau_{rr}}{\partial r} + \frac{1}{r}\frac{\partial \tau_{r\phi}}{\partial \phi} - \frac{\tau_{\phi\phi}}{r}}_{V_r}, \tag{2.3}$$

$$\frac{\partial \rho u_\phi}{\partial t} + \frac{\partial \rho u_\phi u_x}{\partial x} + \frac{1}{r}\frac{\partial r \rho u_\phi u_r}{\partial r} + \frac{1}{r}\frac{\partial \rho u_\phi u_\phi}{\partial \phi} + \frac{\rho u_r u_\phi}{r} = -\frac{1}{r}\frac{\partial p}{\partial \phi}$$

$$\underbrace{+\frac{\partial \tau_{x\phi}}{\partial x} + \frac{1}{r}\frac{\partial r \tau_{r\phi}}{\partial r} + \frac{1}{r}\frac{\partial \tau_{\phi\phi}}{\partial \phi} + \frac{\tau_{r\phi}}{r}}_{V_\phi}, \quad (2.4)$$

$$\frac{\partial E}{\partial t} + \frac{\partial (E+p)u_x}{\partial x} + \frac{1}{r}\frac{\partial r(E+p)u_r}{\partial r} + \frac{1}{r}\frac{\partial (E+p)u_\phi}{\partial \phi} = -\frac{\partial q_x}{\partial x} - \frac{1}{r}\frac{\partial r q_r}{\partial r} - \frac{1}{r}\frac{\partial q_\phi}{\partial \phi} + \Phi$$

$$+ u_x V_x + u_r V_r + u_\phi V_\phi + u_x f_x, \quad (2.5)$$

$$p = \rho R T. \quad (2.6)$$

They express the conservation of mass density ρ, axial, radial and azimuthal momentum density $\rho u_x, \rho u_r, \rho u_\phi$ and total energy density $E = \rho(C_v T + 0.5\vec{u}.\vec{u})$, and include the thermally perfect gas equation (2.6), where p is pressure, R the gas constant and T the absolute temperature. The corresponding equations in Cartesian coordinates are well known and need not be repeated here. Equation (2.2) contains a homogeneous body force per unit volume f_x, which drives the flow in axial direction. It implies an extra term in the total energy equation (2.5), $u_x f_x$, namely the work done by the body force. Note that the divergence term due to work done by viscous forces is split into two terms, one of them being the kinetic energy dissipation rate Φ. The viscous stresses follow Newton's law and read in cylindrical coordinates:

$$\tau_{xx} = 2\mu\frac{\partial u_x}{\partial x} - \frac{2}{3}\mu\Theta, \quad \tau_{rr} = 2\mu\frac{\partial u_r}{\partial r} - \frac{2}{3}\mu\Theta, \quad \tau_{\phi\phi} = 2\mu\left(\frac{1}{r}\frac{\partial u_\phi}{\partial \phi} + \frac{u_r}{r}\right) - \frac{2}{3}\mu\Theta, \quad (2.7)$$

$$\tau_{xr} = \mu\left(\frac{\partial u_r}{\partial x} + \frac{\partial u_x}{\partial r}\right), \quad \tau_{x\phi} = \mu\left(\frac{\partial u_\phi}{\partial x} + \frac{1}{r}\frac{\partial u_x}{\partial \phi}\right), \quad \tau_{r\phi} = \mu\left(\frac{\partial u_\phi}{\partial r} + \frac{1}{r}\frac{\partial u_r}{\partial \phi} - \frac{u_\phi}{r}\right), \quad (2.8)$$

$$\Theta = \frac{\partial u_x}{\partial x} + \frac{1}{r}\frac{\partial r u_r}{\partial r} + \frac{1}{r}\frac{\partial u_\phi}{\partial \phi}. \quad (2.9)$$

The heat fluxes in (x, r, ϕ) directions satisfy Fourier's law:

$$q_x = -\lambda\frac{\partial T}{\partial x}, \quad q_r = -\lambda\frac{\partial T}{\partial r}, \quad q_\phi = -\lambda\frac{1}{r}\frac{\partial T}{\partial \phi}. \quad (2.10)$$

The dissipation rate Φ has the following form:

$$\Phi = \tau_{xx}\frac{\partial u_x}{\partial x} + \tau_{rr}\frac{\partial u_r}{\partial r} + \tau_{\phi\phi}\left(\frac{1}{r}\frac{\partial u_\phi}{\partial \phi} + \frac{u_r}{r}\right) + \tau_{xr}\left(\frac{\partial u_x}{\partial r} + \frac{\partial u_r}{\partial x}\right)$$

$$+ \tau_{x\phi}\left(\frac{1}{r}\frac{\partial u_x}{\partial \phi} + \frac{\partial u_\phi}{\partial x}\right) + \tau_{r\phi}\left(r\frac{\partial}{\partial r}\left(\frac{u_\phi}{r}\right) + \frac{1}{r}\frac{\partial u_r}{\partial \phi}\right). \quad (2.11)$$

In the viscous stresses, a bulk viscosity is not taken into account, since it has a negligible effect in the flow regimes under consideration. The dynamic viscosity is proportional to the nth power of the temperature, $\mu \propto T^n$, with $n = 0.7$. Specific heats are assumed to be constant at a ratio of $\gamma = C_p/C_v = 1.4$ for air. The Prandtl number $Pr = C_p\mu/k = 0.71$ is kept constant as well. The remaining flow parameters needed to uniquely characterize compressible flow are the Mach and Reynolds numbers. Parameters that are most pertinent to fully developed turbulent channel and pipe

Flow	Re_τ	M_τ	Re_m	M_m
Pipe	245	0.077	3181	1.30
Channel	246	0.078	2986	1.26

TABLE 1. Flow parameters of pipe and channel DNS.

flow are the friction Reynolds and Mach numbers, *viz*

$$Re_\tau = \bar{\rho}_w u_\tau l / \mu_w = l^+, \qquad M_\tau = u_\tau / \sqrt{\gamma R T_w} \qquad (2.12)$$

with the length scale $l = h$, R representing the channel half-width h and the pipe radius R. The mean values of the dynamic viscosity and the speed of sound are computed at constant wall temperature T_w. The mean density at the wall $\bar{\rho}_w$ and the wall shear stress $\bar{\tau}_w$ are a result of the computation. The friction velocity reads, $u_\tau = \sqrt{|\bar{\tau}_w|/\bar{\rho}_w}$. We follow common practice and apply a tilde and an overbar to define Favre and Reynolds averages, respectively, and double and single dashes to specify Favre and Reynolds fluctuations, respectively, e.g. u'', ρ'.

The uniform body force f_x in (2.2) and (2.5) is chosen such that it generates statistically steady fully developed turbulent pipe and channel flow. This is the case when it equals the mean pressure gradient, which is constant normal to the walls. Given homogeneous wall boundary conditions and a computational domain with an axial extent comparable to the largest turbulent scales, the advantage of this approach is that it allows the use of periodic boundary conditions in the simulation for all flow variables in streamwise x direction. In the simulation, p then fluctuates around a mean value along x. Non-dimensionalized with inner variables, the mean pressure gradient is proportional to the inverse of the Reynolds number. For pipe and channel flow, we have

$$-\bar{p}_x^+|_{pipe} = -\frac{\mu_w}{\bar{\rho}_w u_\tau \bar{\tau}_w} \frac{\partial \bar{p}}{\partial x}\bigg|_{pipe} = \frac{2}{Re_\tau}, \qquad (2.13)$$

$$-\bar{p}_x^+|_{channel} = -\frac{\mu_w}{\bar{\rho}_w u_\tau \bar{\tau}_w} \frac{\partial \bar{p}}{\partial x}\bigg|_{ch} = \frac{1}{Re_\tau}. \qquad (2.14)$$

The result for pipe flow will be derived below.

The values of the friction Reynolds and Mach numbers used in our DNS are listed in table 1, along with the corresponding bulk Reynolds and Mach numbers which are defined as

$$Re_m = \bar{\rho}_m \bar{u}_m l / \mu_w, \qquad M_m = \bar{u}_m / \sqrt{\gamma R T_w}. \qquad (2.15)$$

Here $\bar{\rho}_m$, $\bar{u}_m$ are the cross-sectionally averaged mean density and velocity.

We solve the governing equations in a pressure-entropy-velocity form (Sesterhenn 2001) in Cartesian and cylindrical coordinates (see Ghosh, Sesterhenn & Friedrich 2008 for details). High-order numerical schemes are used to integrate these equations. The fifth-order compact low-dissipation upwind scheme of Adams & Shariff (1996) and the compact sixth-order scheme of Lele (1992) are chosen to discretize convection and molecular transport terms, respectively. A third-order 'low-storage' Runge–Kutta scheme of Williamson (1980) advances the solution in time. The geometric singularity due to $1/r$ terms in the equations is treated by placing no grid point on the cylinder axis (Mohseni & Colonius 2000). The finite-difference schemes have been previously validated for compressible turbulent channel flow by Lechner,
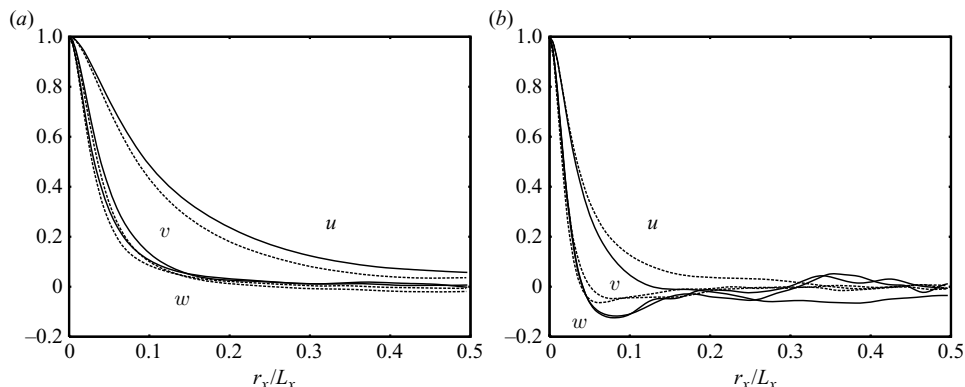
FIGURE 1. Two point correlation of velocity fluctuations in the streamwise direction at $y^+ = 10$ (*a*) and 200 (*b*); pipe (solid line), channel (dashed line).

Sesterhenn & Friedrich (2001) whose results for an $M = 1.5$ case agree very well with those of Coleman *et al.* (1995). Equidistant grids are chosen in streamwise and circumferential (spanwise) directions and grid-clustering is adopted in the wall-normal direction. The computational domains to simulate pipe/channel flow have sizes of $10R \times 2\pi R \times R$ and $4\pi h \times 4\pi h/3 \times 2h$, respectively. In view of recent numerical and experimental investigations dealing with the question whether large outer-scale motions in channel, pipe and boundary layer flows exist and remain passive at all Reynolds numbers or affect the near-wall dynamics, it may be asked whether the chosen computational domains in the streamwise direction are large enough to capture the large-scale structures that exist at $Re_\tau = 245$ and low friction Mach number. From experiments of Morrison *et al.* (2004) in incompressible pipe flow at Reynolds numbers in the range $1500 \leqslant Re_\tau \leqslant 100\,000$, we know that large-scale motions may have maximum wavelengths of approximately $10R$. Similar results were reported by Guala, Hommema & Adrian (2006) for pipe flow in the range $3815 \leqslant Re_\tau \leqslant 7959$. Measurements of streamwise velocity fluctuations in incompressible turbulent boundary layers at $Re_\tau = 7300$ (based on boundary layer thickness δ) by Hutchins & Marusic (2007) reveal inner large-scale structures of 1000 wall units (v/u_τ) in size and outer large scales of 6δ. These scales were deduced from the two peaks in the pre-multiplied streamwise energy spectra. At low Reynolds numbers of the order of 180 these two peaks merge and there is no chance of distinguishing the inner from outer scales. An analogous effect has been found by Abe, Kawamura & Choi (2004) in their DNS of incompressible fully developed channel flow at Re_τ ranging from 180 to 640. Their pre-multiplied spanwise energy spectra show a single peak at $Re_\tau = 180$, but two peaks at $Re_\tau = 640$. They used computational domains of exactly the same size as in the present DNS of channel flow and compared their data with data obtained in smaller domains with the result that only negligibly small differences are found in the mean flow variables and the second-order turbulence statistics. These findings seem to confirm that our simulations properly capture the existing large-scale structures. Finally, the streamwise two-point correlations (figure 1) computed at positions $y^+ = 10$ and 200 decay rapidly within half the channel length and hence validate the domain sizes.

The cylindrical grid for supersonic pipe flow comprises $256 \times 91 \times 128$ points in (x, r, ϕ) directions while the Cartesian grid for supersonic channel flow has $192 \times 151 \times 128$ points in (x, y, z) directions. This translates into mesh sizes in terms
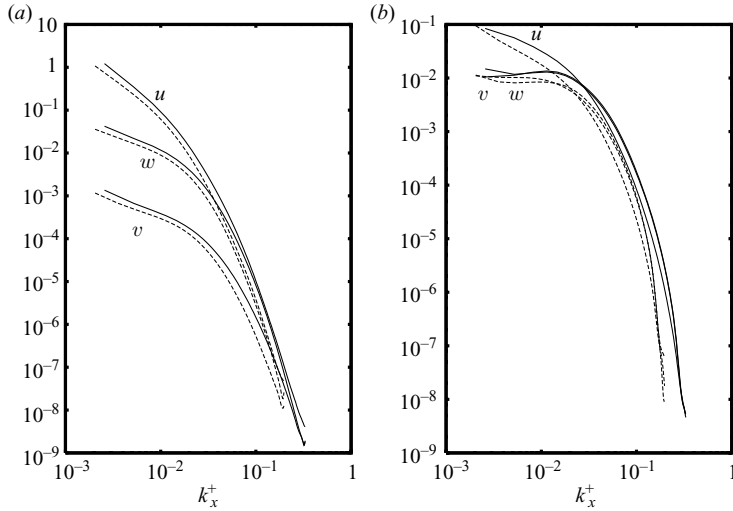
FIGURE 2. One-dimensional streamwise energy spectra ($E^+_{u_i u_i}$) at $y^+ = 10$ (*a*) and 200 (*b*); pipe (solid line), channel (dashed line).

of inner variables of 9.5 (16.1) in streamwise, of 12 (8.05) in circumferential (spanwise) directions and of 0.93 (0.87) nearest to the wall, respectively. The maximum wall-normal mesh sizes which occur near the centreline are $\Delta y^+ = 4.26$ (pipe) and 5.6 (channel). The reader may wonder about the difference in streamwise resolution for channel ($\Delta x^+ = 16.1$) and pipe flow ($\Delta x^+ = 9.5$). The fact is that the grid spacing for the channel is sufficiently small, while that for the pipe is unnecessarily small. The pipe data was used to prescribe inflow conditions for a spatially developing supersonic nozzle flow where higher resolution in the streamwise direction than for fully developed pipe flow was needed (Ghosh *et al.* 2008). The one-dimensional streamwise spectra of the velocity components, shown in figure 2, verify that the flowfields of channel and pipe are properly resolved.

3. Mean flow variables and second-order turbulence statistics

The streamwise pressure gradient has an effect on the whole flow, the importance of which – concerning the turbulence structure – decreases as the Reynolds number increases. To show this, we average the streamwise and radial momentum equations (2.2) and (2.3). For fully developed pipe flow without mean swirling motion ($\tilde{u}_\phi = 0$), we get

$$\frac{1}{r}\frac{\partial}{\partial r}\left(r\bar{\tau}_{xr} - r\overline{\rho u''_x u''_r}\right) = \frac{\partial \bar{p}}{\partial x}, \qquad \bar{\tau}_{xr} \cong \bar{\mu}\frac{\partial \bar{u}_x}{\partial r}, \tag{3.1}$$

$$\frac{1}{r}\frac{\partial}{\partial r}\left(r\overline{\rho u''^2_r}\right) - \frac{\overline{\rho u''^2_\phi}}{r} = -\frac{\partial \bar{p}}{\partial r}. \tag{3.2}$$

The mean viscous stresses are approximated by neglecting correlations with viscosity fluctuations which are small at subsonic and supersonic speeds, as shown by Huang *et al.* (1995). Note also that the Favre averaged radial velocity is exactly zero in (3.2), while the Reynolds averaged component which appears in the radial and circumferential viscous stress is not. It can, however, be assumed small and therefore

$\bar{\tau}_{rr} \cong 0$, $\bar{\tau}_{\phi\phi} \cong 0$. Differentiating (3.2) in axial direction shows that the second derivative $\partial^2 p / \partial r \partial x$ vanishes which means that the mean axial pressure gradient is constant in radial direction. Using the following wall-boundary and symmetry conditions $\bar{\tau}_{xr}|_{r=R} = -\bar{\rho}_w u_\tau^2$, $\overline{\rho u_x'' u_r''}|_{r=R} = \overline{\rho u_x'' u_r''}|_{r=0} = \bar{\tau}_{xr}|_{r=0} = 0$ the momentum equation (3.1) reads in integrated form:

$$\bar{\tau}_{xr} - \overline{\rho u_x'' u_r''} = \frac{r}{2} \frac{\partial \bar{p}}{\partial x} = -\frac{r}{R} \bar{\rho}_w u_\tau^2. \qquad (3.3)$$

A similar equation holds for channel flow in an (x, y, z) coordinate system the origin of which lies on the wall $(y = 0)$. If we replace the radial coordinate by a coordinate y, which is zero at the wall and is defined by $y = R - r$, and substitute $u_x = u$, $u_r = -v$, $u_\phi = w$, we obtain the following linear relations for the total stresses in both flows:

$$\frac{\bar{\mu}}{\mu_w} \frac{d\bar{u}^+}{dy^+} - \frac{\overline{\rho u'' v''}}{|\bar{\tau}_w|} = 1 + y^+ \bar{p}_x^+|_{ch} = 1 - \frac{y^+}{h^+}, \qquad \text{(channel)} \qquad (3.4)$$

$$\frac{\bar{\mu}}{\mu_w} \frac{d\bar{u}^+}{dy^+} - \frac{\overline{\rho u'' v''}}{|\bar{\tau}_w|} = 1 + \frac{1}{2} y^+ \bar{p}_x^+|_{pipe} = 1 - \frac{y^+}{R^+}. \qquad \text{(pipe)} \qquad (3.5)$$

It is now obvious that the effect of the dimensionless pressure gradient (2.13) and (2.14) on the Reynolds shear stress and the turbulence production decreases as the Reynolds number increases. In the limit of high Reynolds number, $Re_\tau = l^+ \gg 1$, (3.4) and (3.5) take a form which is known from zero-pressure-gradient boundary layers.

Using a Taylor series expansion for the Reynolds shear stress in (3.4) and (3.5), the following relation for the dimensionless mean velocity in the viscous sublayers of channel and pipe can be deduced:

$$\left.\begin{aligned}
\frac{\bar{u}}{u_\tau} = \bar{u}^+ = \underbrace{\int_0^{y^+} \frac{\mu_w}{\bar{\mu}} dy^+}_{A} - \underbrace{\int_0^{y^+} \frac{\mu_w}{\bar{\mu} l^+} y^+ dy^+}_{B} + \frac{\sigma}{6} \int_0^{y^+} \frac{\mu_w}{\bar{\mu}} y^{+3} dy^+, \\
\sigma = \frac{3}{|\bar{\tau}_w|} \left[\overline{\frac{\partial \rho u''}{\partial y^+} \frac{\partial^2 v''}{\partial y^{+2}}} \bigg|_w + \overline{\frac{\partial^2 \rho u''}{\partial y^{+2}} \frac{\partial v''}{\partial y^+}} \bigg|_w \right].
\end{aligned}\right\} \qquad (3.6)$$

For incompressible isothermal flow with $\mu_w / \bar{\mu} = 1$, relation (3.6) reduces to a form similar to the asymptotic relation (2.5) given by Nickels (2004) for boundary layer flow, with a linear term, a quadratic (pressure-gradient) term and a fourth-order term in y^+. Since the last term is small at subsonic and supersonic speeds, the investigated near-wall channel and pipe flows should, at first sight, behave similarly, for equal friction Reynolds and Mach numbers. A comparison of viscous and Reynolds shear stresses and total stresses for the flow parameters given in table 1 is presented in figure 3. In this and the following figures dotted/solid lines represent channel/pipe flow, respectively. All curves seem to lie on top of each other. Figure 4 shows profiles of the mean velocity $\bar{u}^+(y^+)$ for channel and pipe flow. Terms A and $A + B$ of (3.6) are also plotted for comparison, using channel data. Again, all curves seem to collapse at least in the viscous sublayer. A closer look, however, reveals subtle differences even close to the wall which result from differences in the mean viscosities of channel and pipe flow, as explained below. In the fully turbulent region the channel has a flatter velocity profile than the pipe which points towards distinct differences in the integral parameters. It is interesting to quantify the absolute error to which the DNS statistics
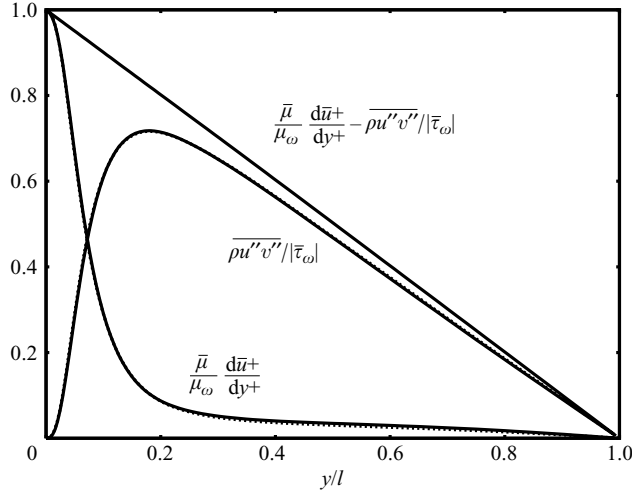
FIGURE 3. Reynolds and viscous shear stress, together with total stress for channel and pipe flow, according to (3.4) and (3.5). Dotted/solid lines represent channel/pipe flow.
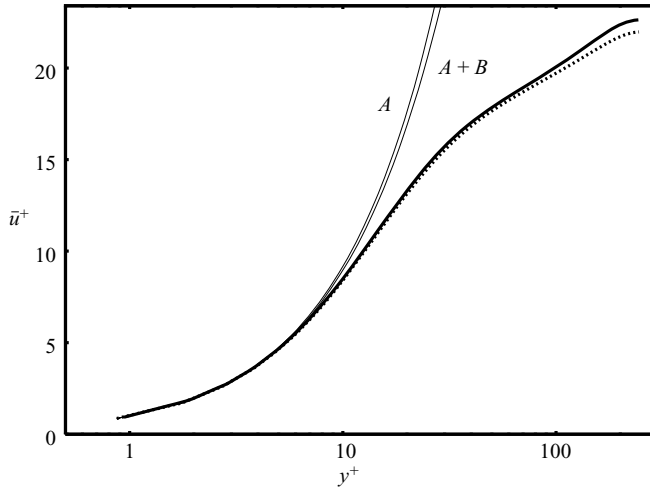

FIGURE 4. Mean velocity $\bar{u}^+$ for channel and pipe flow compared with the terms A and $A + B$ of (3.6) for channel. Dotted/solid lines represent channel/pipe flow.

satisfy the integrated momentum equations (3.4) and (3.5). Figure 5 demonstrates that the maximum absolute errors in the channel and the pipe do not exceed values of 0.004.

Using the van Driest transformation,

$$\bar{u}_{VD}^+ = \int_0^{\bar{u}^+} \sqrt{\frac{\bar{\rho}}{\bar{\rho}_w}} \, d\bar{u}^+, \tag{3.7}$$

the mean velocity profiles tend towards log-laws with marginally different gradients and constants in both flows (see figure 6).

We now integrate the radial mean momentum equation (3.2) and use the coordinate and velocity transformations that led to (3.5) to obtain an expression for the
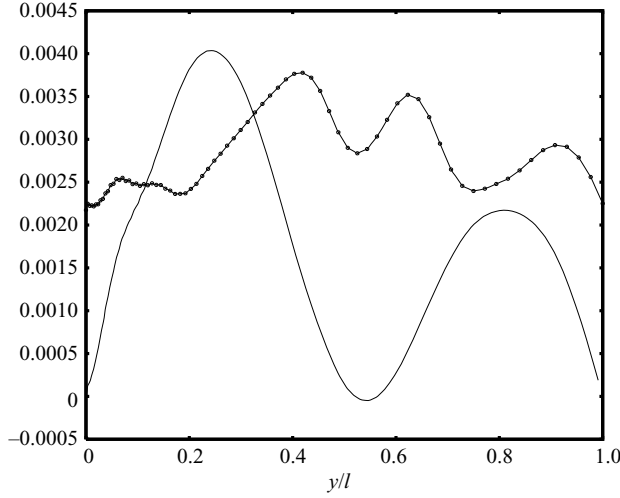
FIGURE 5. The residual of all terms of (3.4) and (3.5) represents the absolute error to which the DNS statistics satisfy the integrated mean momentum equation (channel: curve with circles).
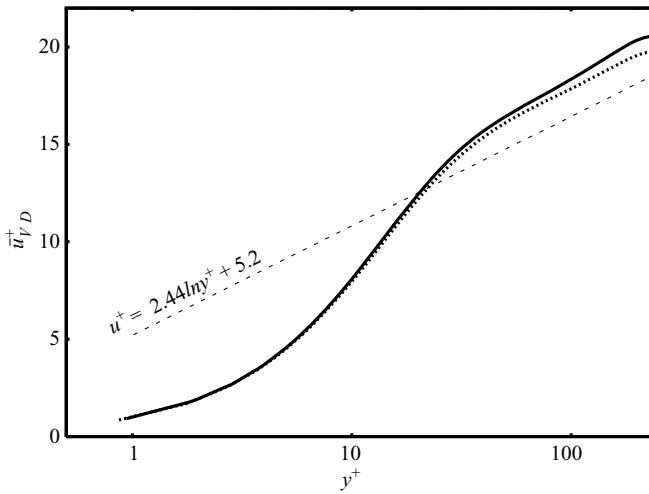

FIGURE 6. Van Driest transformed mean velocity versus y^+. Dotted/solid lines represent channel/pipe flow.

wall-normal pressure variation in the pipe. An analogous expression holds for channel flow, *viz*

$$\bar{p} = \bar{p}_w - \overline{\rho v'' v''}, \quad \text{(channel)} \tag{3.8}$$

$$\bar{p} = \bar{p}_w - \overline{\rho v'' v''} - \int_0^{y/R} (\overline{\rho v'' v''} - \overline{\rho w'' w''}) \frac{\mathrm{d}(y/R)}{1 - y/R}. \quad \text{(pipe)} \tag{3.9}$$

The equations reveal an important qualitative difference between pipe and channel flow resulting from the transverse curvature term. Plots of these profiles in figure 7, show indeed characteristic differences which seem small in this specific normalization. They amount to less than 1 % of the wall pressure, but have a more sensible effect
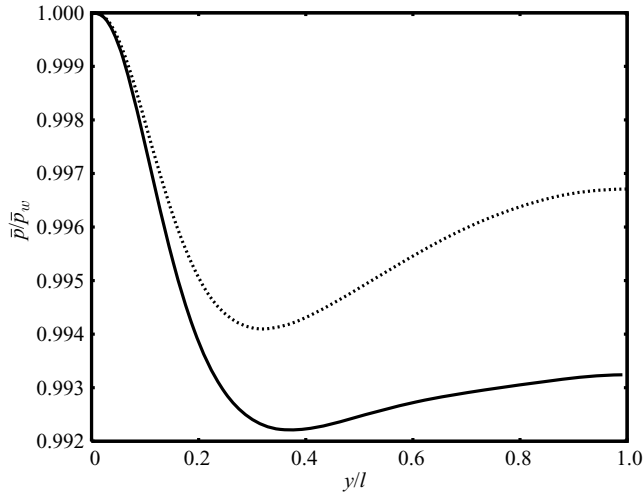
FIGURE 7. Mean pressure normalized with wall pressure. Dotted/solid lines represent
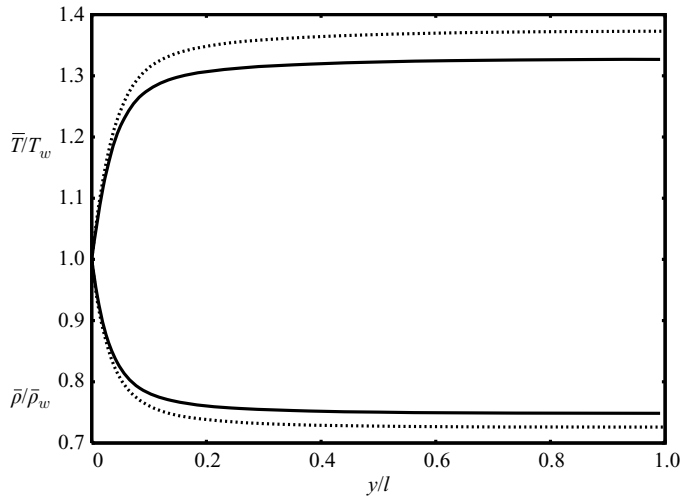channel/pipe flow.

FIGURE 8. Mean density and temperature in channel and pipe flow, normalized with wall
values. Dotted/solid lines represent channel/pipe flow.

on the transverse Reynolds stresses, measured in terms of the wall shear stress, as will be seen later. A key to the understanding of fully developed compressible turbulent channel and pipe flow lies in the rapid wall-normal changes in mean fluid properties, $\bar{\rho}$ and $\bar{T}$, caused by viscous heating. In figure 8 we compare mean density and temperature profiles, normalized with wall values, rather than viscosity profiles. The mean viscosity behaves like the mean temperature ($\mu \propto T^n$), rises steeply in the wall layer and has a plateau in the core (Foysi *et al.* 2004). Obviously, density and temperature differ in both flows at any distance from the wall and the question is why this is so. In order to clarify this, we study the mean internal energy equations,

integrated from the wall to a position y:

$$
\left(\underbrace{\bar{\lambda}\frac{\partial \bar{T}}{\partial y}}_{MHF} - \underbrace{C_v\overline{\rho v''T''}}_{THF}\right) + \underbrace{\bar{q}_w}_{WHF} = -\int\limits_0^y \left(\underbrace{\bar{\mu}\left(\frac{\partial \bar{u}}{\partial y}\right)^2}_{DD} + \underbrace{\epsilon}_{TD} - \underbrace{\bar{p}\frac{\partial \bar{v}}{\partial y}}_{MPD} - \underbrace{\overline{p'd'}}_{PDC}\right)dy, \quad \text{(channel)}
$$

(3.10)

$$
\left(1-\frac{y}{R}\right)\left(\bar{\lambda}\frac{\partial \bar{T}}{\partial y} - C_v\overline{\rho v''T''}\right) + \bar{q}_w = -\int\limits_0^y \left(1-\frac{y}{R}\right)\left(\bar{\mu}\left(\frac{\partial \bar{u}}{\partial y}\right)^2 + \epsilon\right.
$$

$$
\left. - \frac{\bar{p}}{\left(1-\frac{y}{R}\right)}\frac{\partial\left(1-\frac{y}{R}\right)\bar{v}}{\partial y} - \overline{p'd'}\right)dy. \quad \text{(pipe)} \quad (3.11)
$$

The labels of various terms in (3.10) have the following meaning: *MHF*, mean molecular heat flux; *THF*, turbulent heat flux; *WHF*, wall heat flux; *DD*, direct dissipation; *TD*, turbulent dissipation; *MPD*, mean pressure–dilatation; *PDC*, pressure–dilatation correlation.

In these equations we have, in analogy to the viscous stress in (3.1), approximated the mean molecular heat fluxes, neglecting correlations with fluctuations of the thermal conductivity.

From the mean total energy equations, for channel and pipe flow, integrated from the wall to the centreline, we equate the heat transfer into the walls equal to the total pressure work done:

$$
\bar{q}_w = h\bar{u}_m\frac{\partial \bar{p}}{\partial x} = -\bar{u}_m|\bar{\tau}_w|, \quad \bar{u}_m = \frac{1}{h}\int\limits_0^h \bar{u}\,dy, \quad \text{(channel)} \quad (3.12)
$$

$$
\bar{q}_w = \frac{R}{2}\bar{u}_m\frac{\partial \bar{p}}{\partial x} = -\bar{u}_m|\bar{\tau}_w|, \quad \bar{u}_m = \frac{2}{R^2}\int\limits_0^R r\bar{u}\,dr. \quad \text{(pipe)} \quad (3.13)
$$

Normalizing (3.11) with the reference quantities $u_\tau, \bar{\rho}_w, T_w, \bar{\tau}_w, \mu_w, \lambda_w$ for mean values of velocity, density, temperature, pressure, viscosity and thermal conductivity at the wall, we obtain

$$
\left(1-\frac{y^+}{R^+}\right)\left(\frac{\gamma}{Pr}\frac{\bar{\lambda}}{\lambda_w}\frac{\partial \bar{T}/T_w}{\partial y^+} - \frac{\overline{\rho v''T''}}{\bar{\rho}_w u_\tau T_w}\right) + \gamma B_q = -\gamma(\gamma-1)M_t^2\int\limits_0^y\left(1-\frac{y^+}{R^+}\right)
$$

$$
\left(\frac{\bar{\mu}}{\mu_w}\left(\frac{\partial \bar{u}^+}{\partial y^+}\right)^2 + \epsilon^+ - \frac{\bar{p}^+}{\left(1-\frac{y^+}{R^+}\right)}\frac{\partial\left(1-\frac{y^+}{R^+}\right)\bar{v}^+}{\partial y^+} - \overline{p'd'}^+\right)dy^+. \quad (3.14)
$$

This equation which has to be integrated a second time to obtain the mean temperature distribution in the pipe, $\bar{T}/T_w$, contains on its left-hand side the mean molecular heat flux, the turbulent heat flux and the heat flux into the wall, in terms of the non-dimensional heat flux, $B_q = \bar{q}_w/(\bar{\rho}_w C_p u_\tau T_w)$ (Bradshaw 1977). The right-hand side comprises the integrated effects of direct and turbulent kinetic energy dissipation
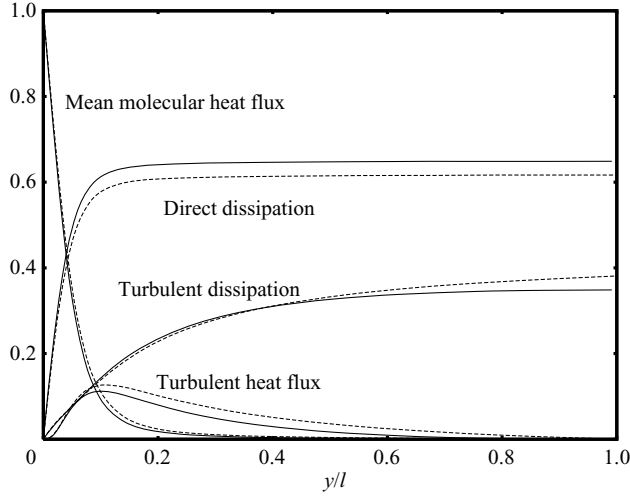
FIGURE 9. Profiles of mean molecular and turbulent heat fluxes and of the integrated effects of direct and turbulent dissipation rates, normalized with the wall heat flux, for channel and pipe flow, according to (3.14). Dotted/solid lines represent channel/pipe flow.

($\epsilon^+ = \epsilon \mu_w/\bar{\tau}_w^2$) and mean pressure-dilatation as well as pressure-dilatation correlation ($(\overline{p'd'})^+ = \overline{p'd'}\mu_w/\bar{\tau}_w^2$). The latter effects are known to be negligibly small up to supersonic speeds (Coleman *et al.* 1995; Huang *et al.* 1995). An equation, similar to (3.14) can be derived for channel flow, just by setting the brackets, $(1 - y^+/R^+)$, in (3.14) equal to 1. Figure 9 contains profiles of the relevant terms in (3.14) for both flows, normalized with the wall heat fluxes. At a certain position $y/h = 0.15$ in the channel, the mean molecular and turbulent heat fluxes surpass those in the pipe at y/R. In contrast to this is the integrated direct dissipation rate everywhere in the channel lower than in the pipe, as a result of lower mean velocity gradients. The integrated turbulent dissipation rate is lower in the wall-layer of the channel, but overshoots that of the pipe in the core region ($y/l > 0.4$). The reason why the molecular heat flux in the pipe is lower than that in the channel is partly also due to transverse curvature. This effect is demonstrated in figure 10, where, besides the two terms for the molecular fluxes in channel and pipe, the term for pipe flow has been plotted in a modified form by setting the factor $(1 - y/R)$ equal to 1 (dashed-dotted curve). Since this curve approaches that for channel flow, it is shown that transverse curvature has an impact on the mean molecular heat flux, and of course on the remaining terms as well.

Now that the reasons for the differences in mean temperature, density and pressure ($\bar{p}/\bar{p}_w \cong \bar{\rho}\bar{T}/(\bar{\rho}_w T_w)$, non-dimensional correlations, $\overline{\rho'T'}/(\bar{\rho}_w T_w)$, are small) between channel and pipe flow are clarified, we present profiles of the three normal Reynolds stresses in figures 11–13, versus the semilocal coordinate, $y^* = y^+ \mu_w/\bar{\mu}\sqrt{\bar{\rho}/\bar{\rho}_w}$ of Huang *et al.* (1995). These stresses are normalized with $|\bar{\tau}_w|$ like the shear stresses in (3.4) and (3.5).

It is interesting to note that in the wall layer of the pipe each of the normal Reynolds stresses collapses onto the corresponding curve for the channel. While the peak values of the streamwise and spanwise (circumferential) stresses still pretty much coincide, those of the wall-normal Reynolds stress do not. Furthermore, we observe differences between channel and pipe flow in their fully turbulent regions, especially for the
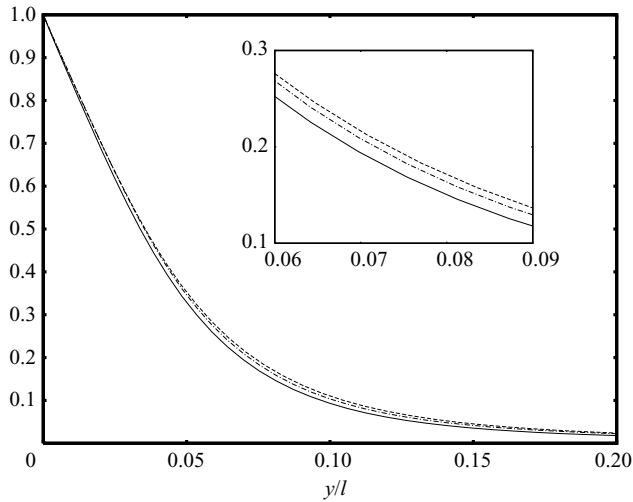
FIGURE 10. Near-wall profiles of the mean molecular heat fluxes for channel (dashed line) and pipe flow (solid line), according to (3.14). The dash-dotted curve represents the mean molecular heat flux in the pipe with the factor $(1 - y/R)$ set to 1. A zoom of a region of the curves is shown in inset.
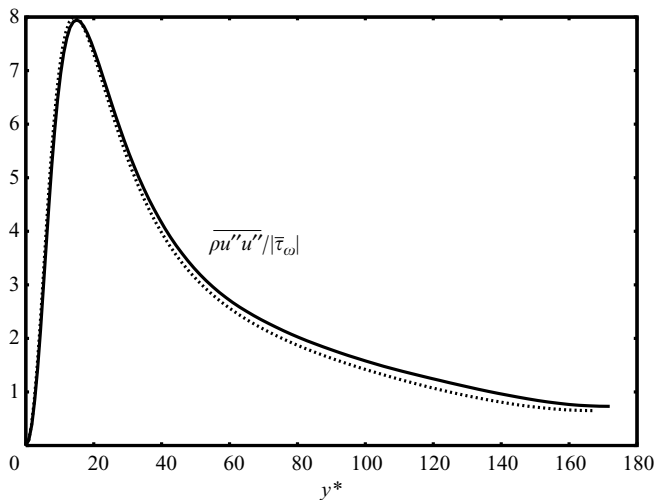

FIGURE 11. Streamwise Reynolds stress versus y^*. Dotted/solid lines represent channel/pipe flow.

wall-normal and spanwise (circumferential) stresses. An explanation for this behaviour has to start from the Reynolds stress transport equations. Anticipating differences in the pressure–strain correlations, we present profiles of the root mean square (RMS) pressure fluctuations in figure 14, normalized with the wall shear stress. The pressure fluctuations in the channel lie consistently below those for the pipe. Even the wall value is roughly 10 % lower. For comparison we have included RMS pressure fluctuations for incompressible pipe flow at a friction Reynolds number of $R^+ = 180$, obtained in the DNS of Wu and Moin (2008). Although our Reynolds number is higher ($R^+ = 245$), the peak pressure fluctuation in the supersonic pipe is lower, due to the decrease in mean density, a Mach number effect that has been explained for
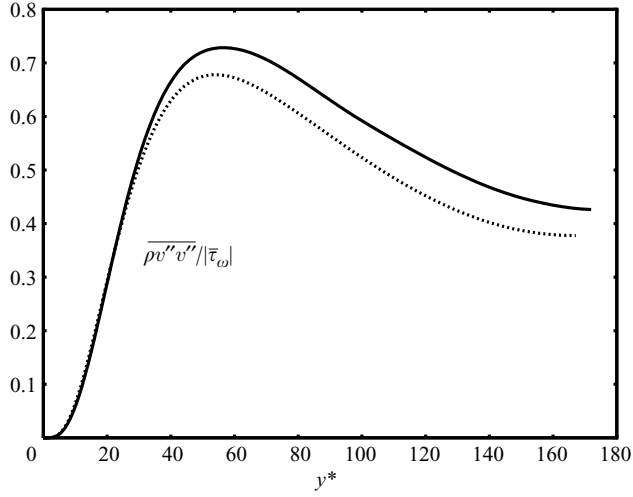
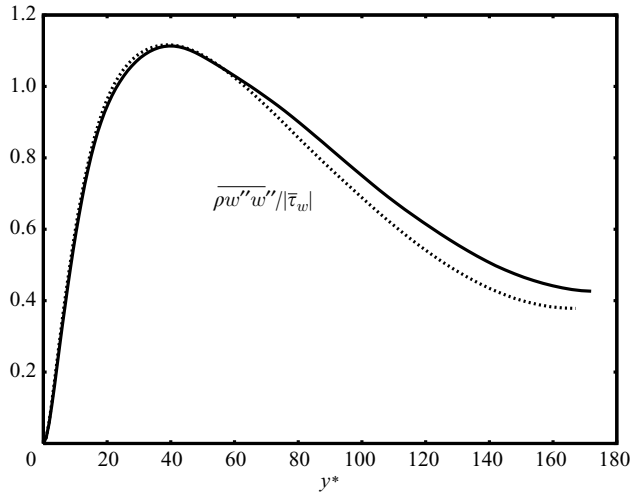FIGURE 12. Wall-normal Reynolds stress versus y^*. Dotted/solid lines represent channel/pipe flow.

FIGURE 13. Spanwise (circumferential) Reynolds stress versus y^*. Dotted/solid lines represent channel/pipe flow.

channel flow by Foysi *et al.* (2004). The wall value, on the other hand is slightly higher than its incompressible counterpart, due to the higher Reynolds number. The three components of the RMS vorticity fluctuations are defined as follows for Cartesian and cylindrical coordinates, using the transformation $y = R - r$, $u'_x = u'$, $v' = -u'_r$, $u'_\phi = w'$:

$$\omega'_x = \frac{\partial w'}{\partial y} - \frac{\partial v'}{\partial z}, \quad \omega'_y = \frac{\partial u'}{\partial z} - \frac{\partial w'}{\partial x}, \quad \omega'_z = \frac{\partial v'}{\partial x} - \frac{\partial u'}{\partial y}, \quad \text{(channel)} \quad (3.15)$$
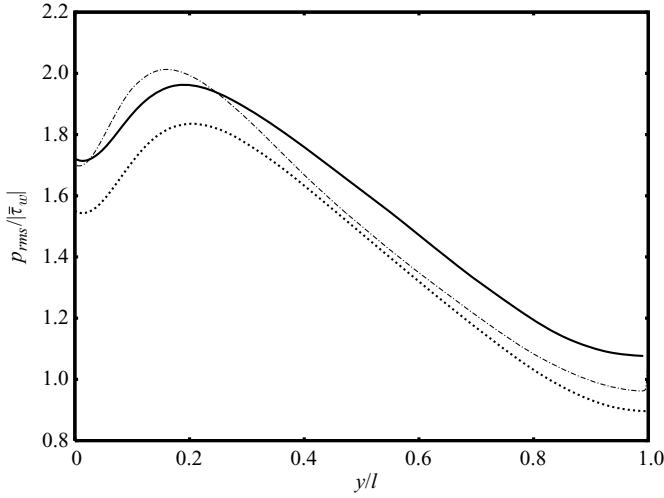
FIGURE 14. RMS pressure fluctuations normalized with the wall shear stress. Solid and dotted lines represent compressible pipe and channel flow, respectively. The dashed-dotted line is for incompressible pipe flow (Wu & Moin 2008, with kind permission of the authors).
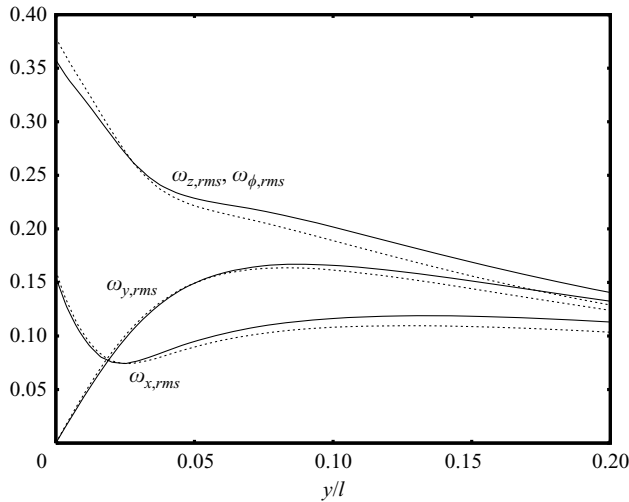

FIGURE 15. RMS vorticity fluctuations, normalized with the friction velocity squared and the wall viscosity. Dotted/solid lines represent channel/pipe flow.

$$\omega'_x = \frac{1}{R-y}\frac{\partial v'}{\partial \phi} - \frac{1}{(1-y/R)}\frac{\partial (1-y/R)w'}{\partial y}, \quad \omega'_y = \frac{1}{R-y}\frac{\partial u'}{\partial \phi} - \frac{\partial w'}{\partial x},$$

$$\omega'_\phi = \frac{\partial u'}{\partial y} - \frac{\partial w'}{\partial x}. \quad \text{(pipe)} \quad (3.16)$$

They are plotted in figure 15, normalized with the friction velocity squared and the viscosity at wall temperature. Here, again, does the fully turbulent flow in the channel core produce weaker vorticity fluctuations than that of the pipe. The opposite is true for the spanwise component close to the wall.

4. Reynolds stress transport equation

For fully developed pipe flow the transport equations for the normal stresses $\overline{\rho u'' u''}$, $\overline{\rho v'' v''}$, $\overline{\rho w'' w''}$ and the shear stress $\overline{\rho u'' v''}$ read, respectively:

$$
0 = \underbrace{-2\overline{\rho u'' v''}\frac{\partial \tilde{u}}{\partial y}}_{P_{xx}} \underbrace{-\frac{1}{(1-y/R)}\frac{\partial (1-y/R)\overline{\rho u'' u'' v''}}{\partial y}}_{TT_{xx}} + \underbrace{\frac{2}{1-y/R}\frac{\partial (1-y/R)\overline{\tau'_{xy}u''}}{\partial y}}_{VD_{xx}} + \underbrace{2\overline{p'\frac{\partial u''}{\partial x}}}_{PS_{xx}}
$$

$$
\underbrace{-2\overline{\tau'_{xx}\frac{\partial u''}{\partial x}} - 2\overline{\tau'_{xy}\frac{\partial u''}{\partial y}} - \frac{2}{R-y}\overline{\tau'_{x\phi}\frac{\partial u''}{\partial \phi}}}_{DS_{xx}} + \underbrace{2\overline{u''}\left(\frac{1}{(1-y/R)}\frac{\partial (1-y/R)\bar{\tau}_{xy}}{\partial y} - \frac{\partial \bar{p}}{\partial x}\right)}_{M_{xx}},
$$

$$(4.1)$$

$$
0 = \underbrace{-\frac{1}{(1-y/R)}\frac{\partial (1-y/R)\overline{\rho v'' v'' v''}}{\partial y} - \frac{2}{R-y}\overline{\rho v'' w'' w''}}_{TT_{yy}}
$$

$$
\underbrace{-\frac{2}{(1-y/R)}\frac{\partial (1-y/R)\overline{p' v''}}{\partial y} + \frac{2}{(1-y/R)}\frac{\partial (1-y/R)\overline{\tau'_{yy}v''}}{\partial y}}_{PD_{yy}/VD_{yy}}
$$

$$
\underbrace{+\frac{2}{(1-y/R)}\overline{p'\frac{\partial (1-y/R)v''}{\partial y}}}_{PS_{yy}} \underbrace{-2\overline{\tau'_{yx}\frac{\partial v'}{\partial x}} - 2\overline{\tau'_{yy}\frac{\partial v'}{\partial y}} - \frac{2}{R-y}\overline{\tau'_{y\phi}\frac{\partial v''}{\partial \phi}}}_{DS_{yy}} + 2\frac{\overline{v''\tau'_{\phi\phi}}}{R-y}
$$

$$
\underbrace{+2\overline{v''}\left(\frac{1}{(1-y/R)}\frac{\partial (1-y/R)\bar{\tau}_{yy}}{\partial y} + \frac{\bar{\tau}_{\phi\phi}}{R-y} - \frac{\partial \bar{p}}{\partial y}\right)}_{M_{yy}},
$$

$$(4.2)$$

$$
0 =
$$

$$
\underbrace{-\frac{1}{(1-y/R)}\frac{\partial (1-y/R)\overline{\rho v'' w'' w''}}{\partial y} + \frac{2}{(R-y)}\overline{\rho v'' w'' w''}}_{TT_{\phi\phi}} + \underbrace{\frac{2}{(1-y/R)}\frac{\partial (1-y/R)\overline{\tau'_{y\phi}w''}}{\partial y}}_{VD_{\phi\phi}}
$$

$$
\underbrace{+\frac{2}{(R-y)}\overline{p'\frac{\partial w''}{\partial \phi}}}_{PS_{\phi\phi}} \underbrace{-2\overline{\tau'_{x\phi}\frac{\partial w''}{\partial x}} - 2\overline{\tau'_{y\phi}\frac{\partial w''}{\partial y}} - \frac{2}{(R-y)}\overline{\tau'_{\phi\phi}\frac{\partial w''}{\partial \phi}}}_{DS_{\phi\phi}} - 2\frac{\overline{w''\tau'_{y\phi}}}{R-y}
$$

$$
\underbrace{+2\overline{w''}\left(\frac{1}{(1-y/R)}\frac{\partial (1-y/R)\bar{\tau}_{y\phi}}{\partial y} - \frac{1}{R-y}\bar{\tau}_{y\phi}\right)}_{M_{\phi\phi}},
$$

$$(4.3)$$

$$0 = \underbrace{\overline{\rho v'' v''} \frac{\partial \widetilde{u}}{\partial y}}_{P_{xy}} + \underbrace{\frac{1}{(1 - y/R)} \frac{\partial (1 - y/R)\overline{\rho v'' u'' v''}}{\partial y} + \frac{1}{R - y} \overline{\rho u'' w'' w''}}_{TT_{xy}}$$

$$+ \underbrace{\frac{1}{(1 - y/R)} \frac{\partial (1 - y/R)\overline{p' u''}}{\partial y}}_{PD_{xy}} - \underbrace{\overline{p'\left(\frac{\partial v''}{\partial x} + \frac{1}{(1 - y/R)} \frac{\partial (1 - y/R)u''}{\partial y} \right)}}_{PS_{xy}}$$

$$- \underbrace{\frac{1}{(1 - y/R)} \frac{\partial (1 - y/R)(\overline{\tau'_{xy} v''} + \overline{\tau'_{yy} u''})}{\partial y}}_{VD_{xy}}$$

$$+ \underbrace{\overline{\tau'_{xx} \frac{\partial v''}{\partial x}} + \overline{\tau'_{xy} \left(\frac{\partial v''}{\partial y} + \frac{\partial u''}{\partial x} \right)} + \overline{\tau'_{yy} \frac{\partial u''}{\partial y}} + \frac{1}{R - y} \left(\overline{\tau'_{x\phi} \frac{\partial v''}{\partial \phi}} + \overline{\tau'_{y\phi} \frac{\partial u''}{\partial \phi}} \right) - \frac{\overline{u'' \tau'_{\phi\phi}}}{R - y}}_{DS_{xy}}$$

$$+ \underbrace{\overline{v''} \left(\frac{\partial \bar{p}}{\partial x} - \frac{1}{(1 - y/R)} \frac{\partial (1 - y/R)\bar{\tau}_{xy}}{\partial y} \right) + \overline{u''} \left(\frac{\partial \bar{p}}{\partial y} - \frac{1}{(1 - y/R)} \frac{\partial (1 - y/R)\bar{\tau}_{yy}}{\partial y} \right)}_{M_{xy}}.$$

$$(4.4)$$

The labels of the various terms in (4.1)–(4.4) have the following meaning: P: production, TT: turbulent transport, PD/VD: pressure and viscous diffusion, PS: pressure–strain rate redistribution, DS: viscous (or turbulent) dissipation, M: mass flux variation (viscous and pressure work).

The second term in TT_{yy}, $TT_{\phi\phi}$ and TT_{xy} is sometimes labelled CR for 'cylindrical coordinate redistribution'. We do not follow this notation and prefer underlining its origin, the convection term. The corresponding Reynolds stress transport equations for channel flow may be obtained from (4.1)–(4.4) by replacing $\partial/r\partial\phi$ by $\partial/\partial z$ and letting $R \to \infty$. When we normalize all terms in the transport equations using $\bar{\tau}_w^2/\bar{\mu}$, as suggested by Foysi *et al.* (2004), we see only a subtle difference in figure 16 between the production terms of channel and pipe flow, at least up to the zone of maximum production. This minor difference might result from gradients of the mean Favre fluctuation which appears in the normalized production term:

$$-2 \frac{\overline{\rho u'' v''}}{|\bar{\tau}_w|} \frac{\bar{\mu}}{\mu_w} \frac{\partial \widetilde{u}^+}{\partial y^+} = -2 \frac{\overline{\rho u'' v''}}{|\bar{\tau}_w|} \frac{\bar{\mu}}{\mu_w} \frac{\partial \bar{u}^+}{\partial y^+} + 2 \frac{\overline{\rho u'' v''}}{|\bar{\tau}_w|} \frac{\bar{\mu}}{\mu_w} \frac{\partial \overline{u''}^+}{\partial y^+}. \qquad (4.5)$$

While the first term on the right-hand side of (4.5) is identical in both flows (cf. figure 3), minor differences can only result from the gradient of the mean Favre fluctuation and the viscosity ratio. However, since $\overline{u''}$ is only of the order of 1% of the bulk velocity $\bar{u}_m$ the second term on the right-hand side of (4.5) is small compared to the first. In the fully turbulent flow region ($y^* > 30$) the source terms P_{xx}, DS_{xx}, PS_{xx} and even the turbulent transport term TT_{xx} (figure 17) show differences between channel and pipe flow, in the sense that the amplitudes of these terms are consistently smaller in the channel. This is, as we have seen, consistent with the observation that the wall-normal and spanwise velocity fluctuations in the channel are lower than in
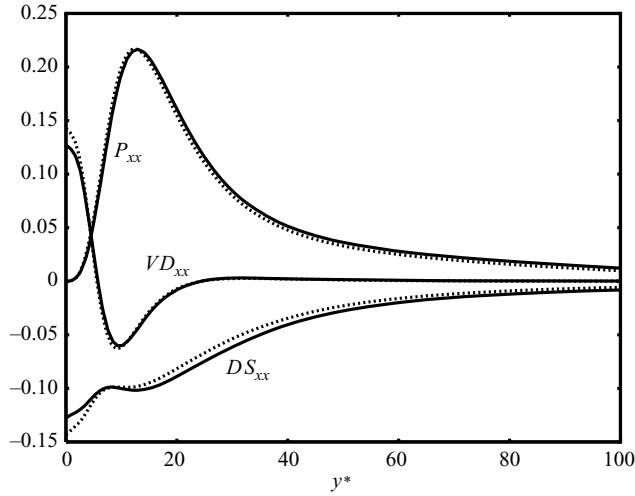
FIGURE 16. Terms of the streamwise Reynolds stress budget versus y^*. Production (P_{xx}), dissipation (DS_{xx}) and viscous diffusion (VD_{xx}). Dotted/solid lines represent channel/pipe flow.
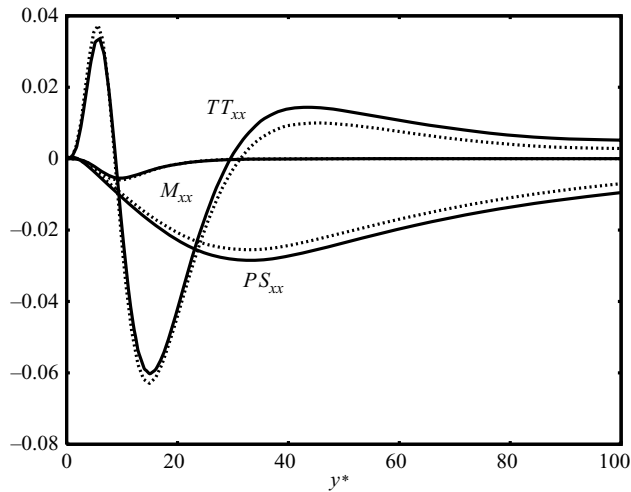

FIGURE 17. Terms of the streamwise Reynolds stress budget versus y^*. Pressure–strain correlation (PS_{xx}), turbulent transport (TT_{xx}), mass flux variation (M_{xx}). Dotted/solid lines represent channel/pipe flow.

the pipe (see figures 12 and 13). Of special importance, in this context, is the fact that the pressure–strain correlation in the channel is reduced compared to that in the pipe. As a consequence the wall-normal and spanwise Reynolds stresses will receive less energy than the corresponding stresses in the pipe. This is indeed the case as seen in figures 18 and 19. For completeness, we present the Reynolds shear stress budget in figure 20 and note consistently smaller amplitudes in the source terms for channel flow.

We would like to touch on a further interesting point observed close to the wall and especially pronounced in the streamwise Reynolds stress balance, figure 16, namely the fact that the viscous diffusion and dissipation terms in the channel have higher amplitudes than those in the pipe. To confirm that this is a physical effect, we write
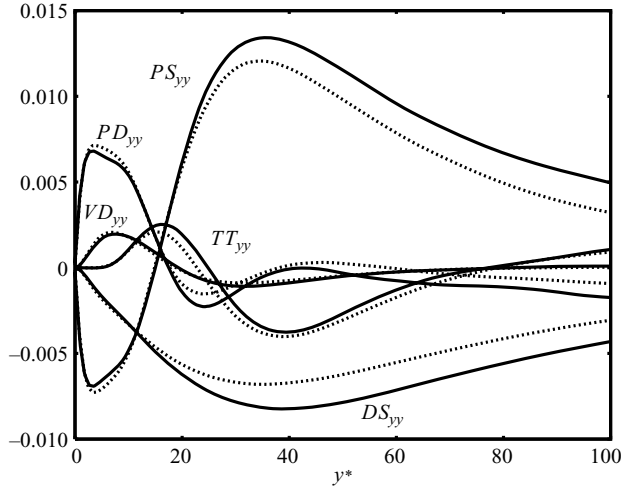
FIGURE 18. Terms of the wall-normal Reynolds stress budget versus y^*. Not all terms are plotted for better visibility. Dotted/solid lines represent channel/pipe flow.

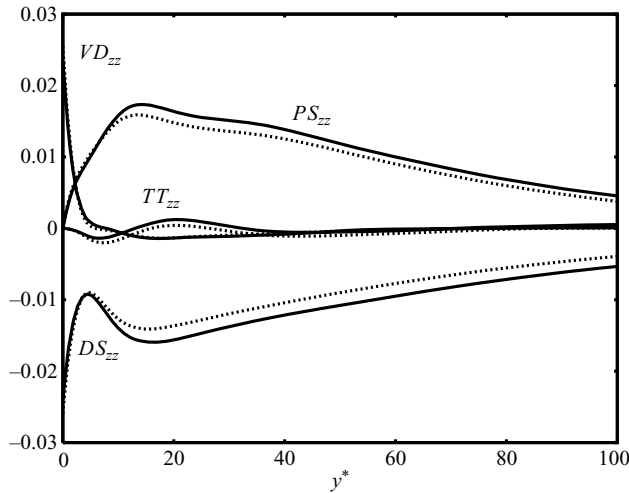

FIGURE 19. Terms of the spanwise (circumferential) Reynolds stress budget versus y^*. Not all terms are plotted for better visibility. Dotted/solid lines represent channel/pipe flow.

down the viscous diffusion term and split it into two terms as follows:

$$VD_{xx} = 2\left(\frac{\partial \overline{\tau'_{xy}u''}}{\partial y} - \frac{\overline{\tau'_{xy}u''}}{R - y}\right). \tag{4.6}$$

The contribution of the term $2(\overline{\tau'_{xy}u''}/R - y)$ which appears only in the pipe flow is small particularly near the wall. So, we focus on the term $2(\partial\overline{\tau'_{xy}u''}/\partial y)$.

The correlation function can be written as $\overline{\tau'_{xy}u''} = \overline{\tau'_{xy}u'}$. Since we have neglected viscosity fluctuations in the definition of the mean viscous shear stress (see (3.1)), we
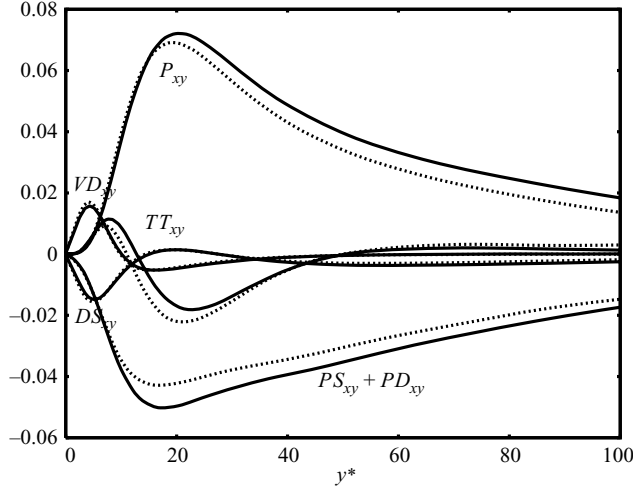
FIGURE 20. Terms of the Reynolds shear stress budget versus y^*. Not all terms are plotted for better visibility. Dotted/solid lines represent channel/pipe flow.

do the same in defining the fluctuating shear stress as

$$\tau'_{xy} \cong \bar{\mu} \left(\frac{\partial v'}{\partial x} + \frac{\partial u'}{\partial y} \right). \tag{4.7}$$

Using (4.7), the correlation function takes the form

$$\overline{\tau'_{xy} u'} \cong \bar{\mu} \left(\frac{\partial \overline{u'^2/2}}{\partial y} - \overline{v' \frac{\partial u'}{\partial x}} \right). \tag{4.8}$$

The term $\bar{\mu} \overline{v' \partial u'/\partial x}$ is negligible.

The viscous diffusion term now reads:

$$V D_{xx} = \left(\frac{\partial \overline{u'^2}}{\partial y} \frac{\partial \bar{\mu}}{\partial y} + \bar{\mu} \frac{\partial^2 \overline{u'^2}}{\partial y^2} \right) \tag{4.9}$$

which leads to the following non-dimensional form at the wall

$$\left. \frac{V D_{xx}}{\bar{\tau}_w^2/\mu} \right|_w = \left. \frac{\partial^2 \overline{u'^2}/u_\tau^2}{\partial y^{+2}} \right|_w . \tag{4.10}$$

Hence, different curvature of the streamwise RMS velocity fluctuations explains why viscous diffusion and dissipation close to a channel wall differ from the corresponding values in the pipe. Figure 21 presents the two terms of (4.9), normalized with $\bar{\tau}_w^2/\bar{\mu}$.

With this effect in mind the near-wall behaviour of the spanwise (circumferential) RMS vorticity fluctuation in figure 15, which is controlled by $\partial u'/\partial y$ close to the wall, makes sense and provides hints for improved low-Reynolds number modelling.

5. Analysis of pressure–strain correlation

We start from an equation for the pressure fluctuation, which is obtained by taking the divergence of the momentum equation, introducing mass conservation and
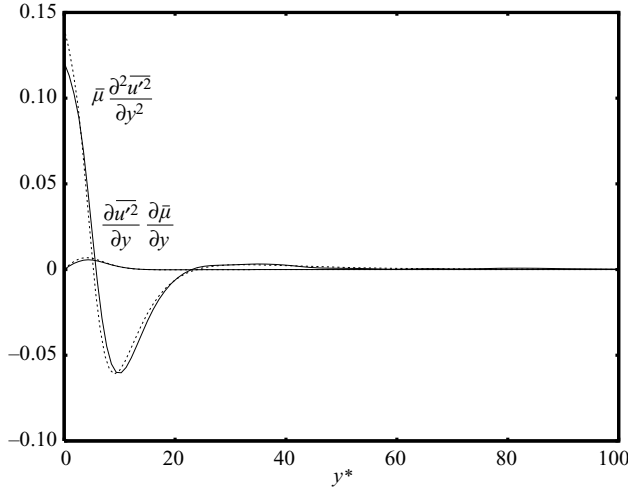
FIGURE 21. Viscous diffusion term split into two terms according to (4.9), normalized with $\bar{\tau}_w^2/\bar{\mu}$ and plotted versus y^*. Dotted/solid lines represent channel/pipe flow.

subtracting the corresponding mean equation, *viz*

$$\nabla^2 p' = -\nabla \cdot \nabla \cdot \left(\rho \vec{u} \cdot \vec{u} - \overline{\rho \vec{u} \cdot \vec{u}} \right) + \frac{\partial^2 \rho'}{\partial t^2} + \nabla \cdot \nabla \cdot \underline{\underline{\tau}}' \tag{5.1}$$

The scalar $\nabla \cdot \nabla \cdot \underline{\underline{C}}$, where $\underline{\underline{C}}$ is either the fluctuating stress tensor $\underline{\underline{\tau}}'$ or a dyad, e.g. $\rho \vec{u}.\vec{u}$ reads in cylindrical coordinates:

$$\nabla \cdot \nabla \cdot \underline{\underline{C}} = \frac{1}{r} \left(\frac{\partial^2 r C_{rr}}{\partial r^2} - \frac{\partial C_{\phi\phi}}{\partial r} + 2 \frac{\partial^2 r C_{rx}}{\partial r \partial x} + 2 \frac{\partial^2 C_{\phi x}}{\partial \phi \partial x} \right)$$
$$+ \frac{1}{r^2} \left(2 \frac{\partial^2 r C_{r\phi}}{\partial r \partial \phi} + \frac{\partial^2 C_{\phi\phi}}{\partial \phi^2} \right) + \frac{\partial^2 C_{xx}}{\partial x^2}. \tag{5.2}$$

Instead of the second temporal derivative of the density fluctuation we use the Galilean invariant second material derivative which reads for fully developed non-swirling pipe flow:

$$\frac{\mathrm{D}^2 \rho'}{\mathrm{D}t^2} = \frac{\partial^2 \rho'}{\partial t^2} + 2\widetilde{u}_x \frac{\partial^2 \rho'}{\partial x \partial t} + \widetilde{u}_x^2 \frac{\partial^2 \rho'}{\partial x^2},$$
$$= \frac{\partial^2 \rho'}{\partial t^2} - \widetilde{u}_x^2 \frac{\partial^2 \rho'}{\partial x^2} - 2\widetilde{u}_x \left[\bar{\rho} \left(\frac{\partial^2 u_r''}{\partial x \partial r} + \frac{1}{r} \frac{\partial^2 u_\phi''}{\partial x \partial \phi} + \frac{\partial^2 u_x''}{\partial x^2} \right) + \frac{1}{r} \frac{\partial r \bar{\rho}}{\partial r} \frac{\partial u_r''}{\partial x} \right]$$
$$- 2\widetilde{u}_x \left(\frac{\partial^2 \rho' u_x''}{\partial x^2} + \frac{1}{r} \frac{\partial^2 r \rho' u_r''}{\partial x \partial r} + \frac{1}{r} \frac{\partial^2 \rho' u_\phi''}{\partial x \partial \phi} \right). \tag{5.3}$$

In (5.1) we now split density and velocities into mean and fluctuating parts and obtain two source terms A_R and A_S which define rapid and slow parts of the pressure, like in incompressible flow, besides the terms B_1, B_2 involving first and second radial

derivatives of mean density and terms C_1–C_3, containing density fluctuations:

$$\nabla^2 p' = \underbrace{-2\bar{\rho}\frac{\partial \widetilde{u}_x}{\partial r}\frac{\partial u_r''}{\partial x}}_{A_R} \underbrace{-\bar{\rho}\left(\frac{1}{r}\frac{\partial^2 r\left(u_r''u_r'' - \overline{u_r''u_r''}\right)}{\partial r^2} + \frac{2}{r^2}\frac{\partial^2 r u_r''u_\phi''}{\partial r \partial \phi} + \frac{1}{r^2}\frac{\partial^2 u_\phi''u_\phi''}{\partial \phi^2}\right)}_{A_S}$$

$$\underbrace{-\bar{\rho}\left(-\frac{1}{r}\frac{\partial\left(u_\phi''u_\phi'' - \overline{u_\phi''u_\phi''}\right)}{\partial r} + \frac{2}{r}\frac{\partial^2 r u_r''u_x''}{\partial r \partial x} + \frac{2}{r}\frac{\partial^2 u_\phi''u_x''}{\partial \phi \partial x} + \frac{\partial^2 u_x''u_x''}{\partial x^2}\right)}_{A_S}$$

$$\underbrace{-\frac{\partial \bar{\rho}}{\partial r}\left[\frac{2}{r}\frac{\partial r\left(u_r''u_r'' - \overline{u_r''u_r''}\right)}{\partial r} + \frac{2}{r}\frac{\partial u_r''u_\phi''}{\partial \phi} - \frac{1}{r}\left(u_\phi''u_\phi'' - \overline{u_\phi''u_\phi''}\right) + 2\frac{\partial u_r''u_x''}{\partial x}\right]}_{B_1}$$

$$\underbrace{-\frac{\partial^2 \bar{\rho}}{\partial r^2}\left(u_r''u_r'' - \overline{u_r''u_r''}\right)}_{B_2} \underbrace{-2\frac{\partial \widetilde{u}_x}{\partial r}\frac{\partial \rho'u_r''}{\partial x}}_{C_1} \underbrace{-\left[\frac{1}{r}\frac{\partial^2 r\left(\rho'u_r''u_r'' - \overline{\rho'u_r''u_r''}\right)}{\partial r^2} + \frac{2}{r^2}\frac{\partial^2 r\rho'u_r''u_\phi''}{\partial r \partial \phi}\right]}_{C_2}$$

$$\underbrace{-\left[\frac{1}{r^2}\frac{\partial^2 \rho'u_\phi''u_\phi''}{\partial \phi^2} - \frac{1}{r}\frac{\partial \rho'\left(u_\phi''u_\phi'' - \overline{\rho'u_\phi''u_\phi''}\right)}{\partial r} + \frac{2}{r}\frac{\partial^2 r\rho'u_r''u_x''}{\partial r \partial x} + \frac{2}{r}\frac{\partial^2 \rho'u_\phi''u_x''}{\partial \phi \partial x} + \frac{\partial^2 \rho'u_x''u_x''}{\partial x^2}\right]}_{C_2}$$

$$\underbrace{-\frac{\mathrm{D}^2\rho'}{\mathrm{D}t^2}}_{C_3} + \underbrace{\nabla\cdot\nabla\cdot\underline{\underline{\tau}}'}_{V}. \tag{5.4}$$

The C_3 term in (5.4), $\mathrm{D}^2\rho'/\mathrm{D}t^2$, leads to a convected, inhomogeneous wave equation for the pressure fluctuation, in principle. Here we assume, as in Foysi *et al.* (2004) for supersonic channel flow, that this term contributes little to p' allowing (5.4) to be interpreted as a Poisson equation for pressure fluctuations. We will, of course, validate this assumption by comparison of the resulting analytical solution with DNS data.

The following Green-function-based analysis of the Poisson equation for p' uses the boundary condition

$$\frac{\partial p'}{\partial r} = \frac{4}{3}\left(\bar{\mu}\frac{\partial^2 u_r'}{\partial r^2} + \frac{\partial \bar{\mu}}{\partial r}\frac{\partial u_r'}{\partial r}\right)$$

at the pipe wall. We denote the right-hand side of (5.4) as $\bar{\rho}\hat{f}'$ and perform a Fourier transformation in the two homogeneous directions to obtain:

$$\frac{\mathrm{d}^2\hat{p}}{\mathrm{d}r^2} + \frac{1}{r}\frac{\mathrm{d}\hat{p}}{\mathrm{d}r} - \left(k_x^2 + \frac{1}{r^2}k_\phi^2\right)\hat{p} = \bar{\rho}\hat{f}. \tag{5.5}$$

Note that the coordinate r and the wavenumbers have been normalized by R. Multiplying (5.5) by r^2 we get,

$$r^2\frac{\mathrm{d}^2\hat{p}}{\mathrm{d}r^2} + r\frac{\mathrm{d}\hat{p}}{\mathrm{d}r} - \left(r^2k_x^2 + k_\phi^2\right)\hat{p} = r^2\bar{\rho}\hat{f} \equiv \bar{\rho}\hat{f}_1. \tag{5.6}$$

The homogeneous equation corresponding to (5.6) is the modified Bessel equation of order k_ϕ which has the general solution

$$\hat{p}(r) = A I_{k_\phi}(k_x r) + B K_{k_\phi}(k_x r),$$

where $I_{k_\phi}(k_x r)$ and $K_{k_\phi}(k_x r)$ are modified Bessel functions of first and second kind, respectively. The constants A and B follow from the boundary conditions. Since, (5.6) is linear, we use the superposition principle to get the final solution.

First, we seek a Green function $G(k_x, k_\phi, r, r_o)$ which satisfies the following equation:

$$r^2 \frac{d^2 G}{dr^2} + r \frac{dG}{dr} - \left(r^2 k_x^2 + k_\phi^2\right) G = r^2 \delta(r - r_o), \qquad (5.7)$$

where r_o is the position of the point source. Equation (5.7) satisfies the homogeneous boundary condition $B_1 = 0$ at $r = 1$. Finiteness of G should be imposed at $r = 0$. Below and above r_o, (5.7) has the following solutions:

$$G_<(k_x, k_\phi, r, r_o) = C I_{k_\phi}(k_x r) + D K_{k_\phi}(k_x r), \quad 0 \leqslant r < r_o,$$
$$G_>(k_x, k_\phi, r, r_o) = A I_{k_\phi}(k_x r) + B K_{k_\phi}(k_x r), \quad r_o < r \leqslant 1,$$

G being finite at $r = 0$, leads to $D = 0$, since $K_{k_\phi}(k_x r)$ goes to infinity at $r = 0$ for some values of k_ϕ. There remain three constants to be evaluated from the following conditions:
(i) Boundary condition at $r = 1$,
(ii) Continuity of G close to $r = r_o$, i.e. $G_< = G_>$,
(iii) Jump condition on G close to $r = r_o$, i.e. $dG_>/dr - dG_</dr = 1/r$ (Stakgold 1979).

After some algebra we get the following solution for G for $k_x \neq 0, k_\phi \neq 0$

$$G_<(k_x, k_\phi, r, r_o) = -\frac{I_{k_\phi}(k_x r_o) I_{k_\phi}(k_x r) K'_{k_\phi}(k_x)}{I'_{k_\phi}(k_x)} + K_{k_\phi}(k_x r_o) I_{k_\phi}(k_x r),$$

$$G_>(k_x, k_\phi, r, r_o) = -\frac{I_{k_\phi}(k_x r_o) I_{k_\phi}(k_x r) K'_{k_\phi}(k_x)}{I'_{k_\phi}(k_x)} + I_{k_\phi}(k_x r_o) K_{k_\phi}(k_x r). \qquad (5.8)$$

Here use is made of the Wroskian

$$I_{k_\phi}(k_x r) K'_{k_\phi}(k_x r) - K_{k_\phi}(k_x r) I'_{k_\phi}(k_x r) = \frac{1}{k_x r} \qquad (5.9)$$

Solutions for the three cases $k_x = 0, k_\phi \neq 0$; $k_x \neq 0, k_\phi = 0$ and $k_x = 0, k_\phi = 0$ can be derived easily and are not included here for brevity. The modified Bessel functions are computed using GNU Scientific Library. Next, we solve the homogeneous equation corresponding to (5.6) satisfying the inhomogeneous boundary condition

$$B_1 = 4/3 \left(\bar{\mu} \frac{\partial^2 \hat{u}_r}{\partial r^2} + \frac{\partial \bar{\mu}}{\partial r} \frac{\partial \hat{u}_r}{\partial r} \right) \quad \text{at} \quad r = 1.$$

The solution of this equation after imposing the finiteness condition at $r = 0$ (as discussed above) and the boundary condition at $r = 1$ is

$$\hat{p}_B = \frac{B_1 I_{k_\phi}(k_x r)}{k_x I'_{k_\phi}(k_x)}.$$

So, using superposition, the solution to (5.6) is

$$\hat{p}(k_x, k_\phi, r) = \int_0^1 G(k_x, k_\phi, r, r_o) \bar{\rho}(r_o) \hat{f}(k_x, k_\phi, r_o) r_o dr_o + \hat{p}_B(k_x, k_\phi, r). \qquad (5.10)$$
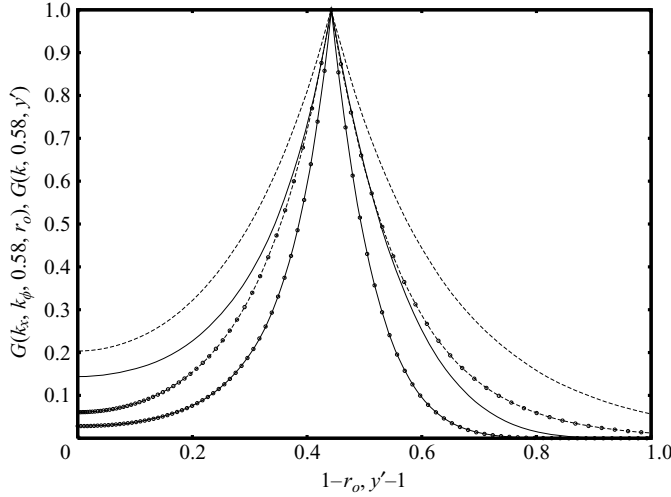
FIGURE 22. Green functions of pipe (solid line) and channel (dashed line) due to a point source located at $y = 0.58$, $r = 0.58$ for different sets of wavenumbers, normalized with their respective maxima. $k_x l = 5$, $k_z l = 9$ (lines); $k_x l = 5$, $k_z l = 15$ (lines with circles).

It is worthwhile to compare the Green function (5.8) with that for the channel flow given below, as described by Kim (1989) and Foysi *et al.* (2004), for two different sets of wavenumbers:

$$G_<(k, y, y') = -\frac{\cosh[k(y'-1)]\cosh[k(y+1)]}{2k\cosh(k)\sinh(k)}, \quad y < y'$$

$$G_>(k, y, y') = -\frac{\cosh[k(y'+1)]\cosh[k(y-1)]}{2k\cosh(k)\sinh(k)}, \quad y > y',$$

where y' is the point source location (y, y' are normalized with channel half-width h and have their origin at the channel centre line in the analysis and in figure 22) and $k = \sqrt{k_x^2 + k_z^2}$.

Figure 22 shows the profiles of $G(k_x, k_\phi, 0.58, r_o)$ and $G(k, 0.58, y')$ for a point source location at $y = 0.58$, $r = 0.58$. As to be expected, the different geometries of pipe and channel flow lead to different decay rates of the Green function away from the source location. The decay rates are faster at higher wavenumbers, indicating that the high-wavenumber content of the source term has a more local effect, in contrast to its low-wavenumber counterpart which affects the pressure fluctuation globally.

The inverse Fourier transform of (5.10) provides the pressure fluctuation in physical space

$$p'(x, r, \phi) = \int_0^1 \bar{\rho}(r_o) G * f'(x, r, \phi, r_o) r_o \mathrm{d}r_o + p'_B(x, r, \phi), \tag{5.11}$$

where $G * f'$ represents the inverse Fourier transform of $G\hat{f}$. From (5.11), the components of the pressure–strain correlation tensor are obtained, e.g.

$$PS_{xx} = \overline{p'\frac{\partial u'}{\partial x}} = \int_0^1 \bar{\rho}(r_o)\overline{G * f'(x, r, \phi, r_o)\frac{\partial u'}{\partial x}} r_o \mathrm{d}r_o + \overline{p'_B \frac{\partial u'}{\partial x}}. \tag{5.12}$$

This result underlines the non-local effect of $\bar{\rho}$ on the pressure–strain correlation.
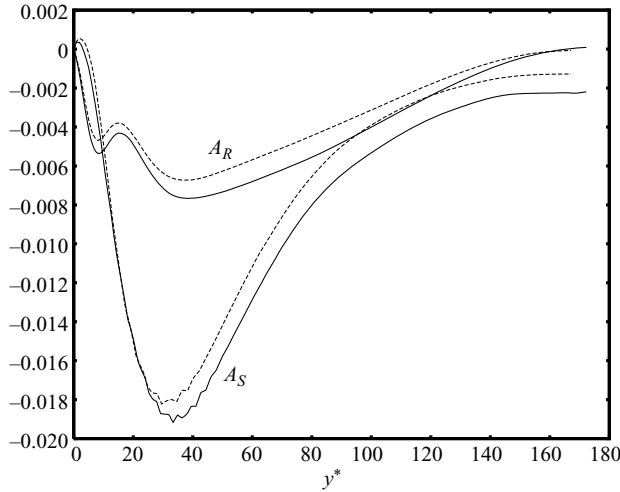
FIGURE 23. Contributions of the rapid term A_R and the slow term A_S to PS_{xx} in pipe (solid line) and channel flow (dashed line).

In (5.12), the quantity $\overline{G * f'(x, r, \phi, r_o) \partial u'/\partial x}$ is obtained numerically by Reynolds averaging the instantaneous values of $G * f' \partial u'/\partial x$. It was shown by Foysi *et al.* (2004) for channel flows, that the terms containing mean density and its wall-normal gradient on the right-hand side of the Poisson equation for p' are the most significant source terms which contribute to PS_{xx}. Because (5.4) (after neglecting the C_3 term) is linear, we first test the contributions of the rapid and the slow terms, A_R and A_S, to PS_{xx}. The result is shown in figure 23 and indicates that the nonlinear or slow term, A_S, dominates over the rapid term in both flows. A_R, on the other hand, reflects the competing effects of the mean velocity gradient close to the wall and of the radial (wall-normal) velocity fluctuation's streamwise gradient away from the wall which explains the double peak behaviour in both flows. The sum of A_R and A_S forms the main contribution to PS_{xx} which is obvious from figure 24, where the combined contribution of A_R, A_S, B_1 and B_2, evaluated using (5.11), is compared to DNS data for pipe (solid curve) and channel flow (dashed curve). Firstly, we note that the overall agreement between the analytical solution (5.12) for the pipe (and an analogous solution for the channel) and the present DNS data is very good, confirming that a variable-density extension of the Poisson equation for p' is sufficient to obtain the pressure–strain term in supersonic pipe and channel flow. The differences between the solutions for the pipe and channel flow is due to the different mean densities in the two flows as well as to the curvature effect on the source terms and Green function in the pipe flow.

6. Conclusions

Comparison of fully developed turbulent compressible channel and pipe flow at equal friction Reynolds number of 245 and friction Mach number of 0.077 (corresponding to supersonic global Mach numbers) based on DNS data reveals more differences than similarities.

The key to the understanding of these differences on a statistical level, which ignores the existence of coherent structures, is transverse curvature which gradually loses importance as the radius of curvature R or equivalently the friction Reynolds number Re_τ increases. Transverse curvature explicitly affects the wall-normal mean pressure
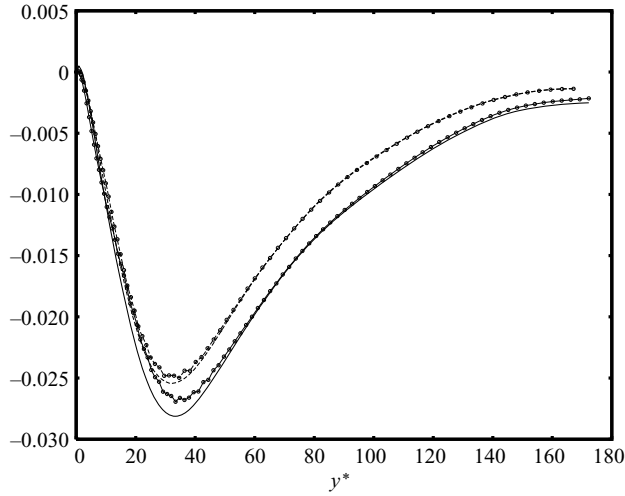
FIGURE 24. Combined contribution of A_R, A_S, B_1 and B_2 to PS_{xx} in pipe and channel flow. Lines with dots are the Green function solutions and the solid and dashed lines are PS_{xx} from DNS for pipe and channel flow, respectively.

distribution (defined in (3.9)) and the mean temperature and density distributions (defined in (3.14)). Although the wall-normal Reynolds stress is already affected by the mean pressure (defined in (3.8) and (3.9)), there is a further mechanism which contributes to differences in Reynolds normal stresses in the channel and the pipe away from the wall, namely turbulent energy redistribution. Transport equations for the normal Reynolds stresses contain pressure–strain correlations which are consistently lower in the channel than in the pipe core, and this is the main reason why the normal stresses in the channel are lower than in the pipe.

The explanation for the observed differences in pressure–strain correlations is provided through a simplified solution for the pressure fluctuations using Green's functions and neglecting wave-propagation effects, which contribute to the pressure fluctuations in the core regions alone, but not to the pressure–strain correlations.

REFERENCES

ABE, H., KAWAMURA, H. & CHOI, H. 2004 Very large-scale structures and their effects on the wall shear-stress fluctuations in turbulent channel flow upto $Re_\tau = 640$. *ASME J. Fluids Engng* **126**, 835–843.

ADAMS, N. A. & SHARIFF, K. 1996 A high-resolution hybrid compact-ENO scheme for shock-turbulence interaction problems. *J. Comput. Phys.* **127**, 27–51.

BIRD, R. B., STEWART, W. E. & LIGHTFOOT, E. N. 1960 *Transport Phenomena*. J. Wiley and Sons.

BRADSHAW, P. 1977 Compressible turbulent shear layers. *Annu. Rev. Fluid Mech.* **9**, 33–52.

CHASSAING, P., ANTONIA, R. A., ANSELMET, F., JOLY, F. & SARKAR, S. 2002 *Variable Density Fluid Turbulence*. Kluwer Academic Press.

COLEMAN, G. N., KIM, J. & MOSER, R. D. 1995 A numerical study of turbulent supersonic isothermal-wall channel flow. *J. Fluid Mech.* **305**, 159–183.

FERNHOLZ, H. H. & FINLEY, P. J. 1976 A critical compilation of compressible turbulent boundary layer data. *AGARDograph 223*.

Foysi, H., Sarkar, S. & Friedrich, R. 2004 Compressibility effects and turbulence scalings in supersonic channel flow. *J. Fluid Mech.* **509**, 207–216.

Gatski, T. B. & Bonnet, J. P. 2009 *Compressibility, Turbulence and High Speed Flow*. Elsevier.

Ghosh, S., Sesterhenn, J. & Friedrich, R. 2008 Large-eddy simulation of supersonic turbulent flow in axisymmetric nozzles and diffusers. *Intl J. Heat Fluid Flow* **29**, 579–590.

Guala, M., Hommema, S. E. & Adrian, R. J. 2006 Large-scale and very-large-scale motions in turbulent pipe flow. *J. Fluid Mech.* **554**, 521–542.

Huang, P. G., Coleman, G. N. & Bradshaw, P. 1995 Compressible turbulent channel flows: DNS results and modelling. *J. Fluid Mech.* **305**, 185–218.

Hutchins, N. & Marusic, I. 2007 Large-scale influences in near-wall turbulence. *Phil. Trans. R. Soc.* A **365**, 647–664.

Kim, J. 1989 On the structure of pressure fluctuations in simulated turbulent channel flow. *J. Fluid Mech.* **205**, 421–451.

Kline, S. J., Cantwell, B. J. & Lilley, G. M. 1982 *Proceedings of the 1980–81 AFOSR-HTTM-Stanford Conference on Complex Turbulent Flows*, vol. 1. Department of Mechanical Engineering, Stanford University.

Lechner, R., Sesterhenn, J. & Friedrich, R. 2001 Turbulent supersonic channel flow. *J. Turbul.* **2**, 1–25.

Lele, S. K. 1992 Compact finite difference schemes with spectral-like resolution. *J. Comput. Phys.* **103**, 16–42.

Lele, S. K. 1994 Compressibiliy effects on turbulence. *Annu. Rev. Fluid Mech.* **26**, 211–254.

Mohseni, K. & Colonius, T. 2000 Numerical treatment of polar coordinate singularities. *J. Comput. Phys.* **157**, 787–795.

Morrison, J. F., McKeon, B. J., Jiang, W. & Smits, A. J. 2004 Scaling of the streamwise velocity component in turbulent pipe flow. *J. Fluid Mech.* **508**, 99–131.

Nickels, T. B. 2004 Inner scaling of wall-bounded flows subject to large pressure gradients. *J. Fluid Mech.* **521**, 217–239.

Nieuwstadt, F. T. M. & Bradshaw, P. 1997 Similarities and differences of turbulent boundary layer, pipe and channel flow. In *Boundary Layer Separation in Aircraft Aerodynamics* (ed. R. A. W. M. Henkes & P. G. Bakker), pp. 15–22. Delft University Press.

Schlichting, H. 1968 *Boundary-Layer Theory*, 6th edn. McGraw-Hill.

Sesterhenn, J. 2001 A characteristic-type formulation of the Navier–Stokes equations for high order upwind schemes. *Comput. Fluids* **30**, 37–67.

Smits, A. J. & Dussauge, J. P. 2006 *Turbulent Shear Layers in Supersonic Flow,* 2nd edn. Springer.

Stakgold, I. 1979 *Green's Functions and Boundary Value Problems*. Wiley Interscience.

Williamson, J. K. 1980 Low-storage Runge–Kutta schemes. *J. Comput. Phys.* **35**, 48–56.

Wosnik, M., Castillo, L. & George, W. K. 2000 A theory for turbulent pipe and channel flows. *J. Fluid Mech.* **421**, 115–145.

Wu, X. & Moin, P. 2008 A direct numerical simulation study on the mean velocity characteristics in turbulent pipe flow. *J. Fluid Mech.* **608**, 81–112.